A Method of Three-Dimensional Thermo-Fluid Simulation of the Receiver of a Standard Parabolic Trough Collector

**M. Islam, Suvash C. Saha, M.A. Karim
and Prasad K.D.V. Yarlagadda**

Abstract A parabolic trough collector (PTC) is the most proven concentrating collector system for indirect steam generation in solar thermal power plants. The receiver of the collector is fabricated enveloping a metal absorber tube using an evacuated glass tube. Depending on the level of evacuation, the glass envelope reduces the convection heat loss from the tube almost to zero. However, sometimes the envelopes are broken, damaged or removed that causes potential convection loss from an open-to-air receiver tube. On the other hand, the solar irradiance profile around the receiver tube is likely to be highly nonuniform. In order to study the heat transfer mechanism of an exposed receiver tube of a standard PTC under the actual optical and environmental conditions, a 3-dimensional Computational Conjugate Heat Transfer (CCHT) model of the receiver tube was developed. The CCHT model was developed applying finite volume technique of computational fluid dynamics integrating with a verified Monte Carlo ray tracing optical model. The CCHT model was verified extensively, and different heat loss models were developed to investigate the heat loss characteristics. The convection heat loss from the outer surface of the receiver tube was observed very high as it was exposed to a high-temperature gradient with its surroundings. Therefore, it is obvious that the receiver tube should be enveloped and evacuated properly. A well-managed and efficiently operated PTC solar energy field could be the best candidate for sustainable energy management for a sustainable future.

Keywords LS2 collector · Parabolic trough collector · Computational fluid dynamics · Conjugate heat transfer modelling · Monte Carlo ray tracing · Fluent

M. Islam (✉) · S.C. Saha (✉) · M.A. Karim · P.K.D.V. Yarlagadda
Faculty of Science and Engineering, School of Chemistry, Physics and Mechanical
Engineering, Queensland University of Technology, Brisbane, QLD 4001, Australia
e-mail: murad99me@yahoo.com

S.C. Saha
e-mail: suvash.saha@qut.edu.au

M. Islam
Department of Mechanical Engineering, Chittagong University of Engineering
and Technology, Chittagong 4349, Bangladesh

1 Introduction

Parabolic trough collector (PTC) is a mature and widely used concentrating collector technology in the solar energy field [1, 2]. A PTC, as shown in Fig. 1, consists of a single axis North–South tracking (parallel to YZ plane) parabolic trough (PT) mirror that focuses solar radiation on to a receiver. The receiver, which, ideally, placed axially along the focal line (along X axis) of the mirror, consists of a receiver tube (RT) and an evacuated glass tube (GT) envelop. The receiver is the main part of the trough collector system that is used to convert incident solar radiation to thermal energy.

The spectral energy harnessing process of the collector involves: incidence of solar radiation on mirror aperture, reflection and concentration of the incident energy onto the outer surface of the receiver tube, and absorption of the radiant energy as thermal energy. Most of the radiant energy is conducted to the inner surface of the receiver tube as thermal energy due to temperature gradient developed by inducing forced convection heat transfer phenomenon [3]. Some suitable Heat Transfer Fluid (HTF) is used to induce the phenomenon. This is an example of a coupled heat transfer problem with complex geometry condition; this, and fairly similar concepts have been studied theoretically as well as experimentally by many researchers.

A buoyancy-driven flow and heat transfer in a narrow annular gap between co-axial, horizontal cylinders have been investigated experimentally and computationally by Vafai et al. [4], Hamad and Khan [5] and Dyko et al. [6] on different occasions.

Borjini and his research group numerically studied the effect of radiation on steady two-dimensional (2D) laminar natural convection in a participating medium between two horizontal con-focal elliptical cylinders by using an elliptic-cylinder coordinates system [7], and unsteady natural convection in a two-dimensional

Fig. 1 Isometric view of a typical PTC (In the figure, PT, GT and RT refer the parabolic trough mirror, glass tube envelop and the receiver tube, respectively)
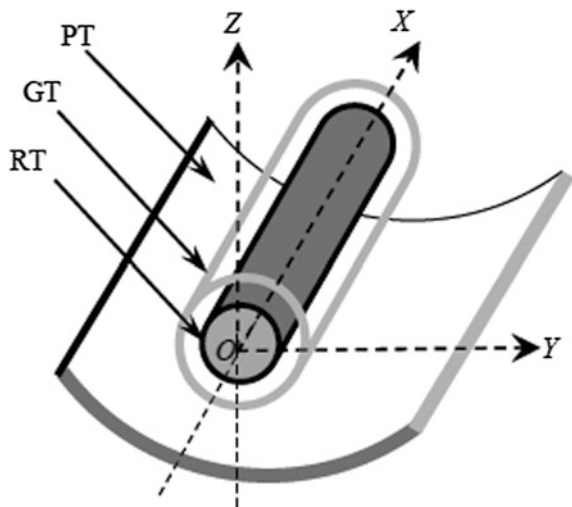
participating medium between two horizontal concentric and vertically eccentric cylinders by using a bi-cylindrical coordinates system [7]. The laminar natural convection in air inside a differentially heated horizontal bare and finned rhombic annulus was studannulus was studied computationallyied computationally by Farinas et al. [8]. Investigations specific to the trough solar collector were also conducted remarkably in recent years.

Dudley et al. [9] investigated the energy performance of the Luz Solar 2 (LS2) PTC performing an extensive experimental procedure. Referring the results for verifications, Forristall [10] developed a detailed one-dimensional and a two-dimensional mathematical models for a PTC to investigate its heat transfer characteristics implementing in an Engineering Equation Solver (EES). An isothermal condition for the glass envelop and a sinusoidal local heat flux distribution for the receiver tube were simulated by Kassem [11], and the free convection heat transfer in the annular space between the receiver tube and the glass envelope was studied. Computational study by Reddy and his research team [12–14] showed that the thermal performance of a PTC with a porous receiver is better than that with a traditional nonporous receiver. Neglecting nonlinearity effect on heat loss, and assuming constant solar radiation, Odeh et al. [15] established a detailed thermal model to calculate the heat loss of trough collector. Later the model was used by Hou et al. [16] to analyse thermal efficiency of a trough system. Effects of the realistic nonuniform heat flux distribution boundary condition on the conjugate heat transfer phenomenon of the collector system have been studied theoretically by different researchers. He et al. [17] simulated the heat transfer process inside the absorber tube and analysed the characteristics under the influence of the nonuniform heat flux distribution around the absorber tube. They coupled a Monte Carlo Ray Tracing (MCRT) optical model with a finite volume Computational Fluid Dynamics (CFD) model to obtain 3D fluid flow fields and temperature distribution for the coupled heat transfer problem in the absorber tube. Tao and He [18] developed a unified computational model for the coupled heat transfer process inside the receiver tube and the annuli space between the receiver tube and the glass envelop of the collector. Islam et al. [19, 20] on different occasions computationally studied the heat transfer mechanism of the receiver tube of a standard PTC.

The foregoing literature review confirms that a plenty of investigations were performed to reveal energy performance and conjugate heat transfer phenomenon of the receiver with evacuated glass envelop, and heat transfer phenomenon inside the annuli space between the receiver and the glass envelop. However, indeed the annuli space is not always evacuated, and many a times the glass envelops are either broken or removed. Again, usually there is no evacuated glass cover around the Concentrating Photovoltaic/Thermal (CPV/T) receiver. Therefore, the receiver is exposed to its surroundings and experiences both free convection and radiation heat losses. This article details a method of 3D Computational Conjugate Heat Transfer (CCHT) model of a bare receiver tube of a standard parabolic trough collector applying Finite Volume (FV) discretization technique of CFD.

The receiver tube of the LS2 PTC from Dudley et al. [9] was modelled and simulated. The irradiance distribution around the receiver tube was calculated

applying a verified MCRT optical model [21, 22] and was integrated with the FV model applying a special MCRT-FV coupling technique. Several test conditions of the bare receiver of the LS2 collector were simulated. As the receiver was bare to the environment, special care was taken in calculating the radiation heat loss and the natural convection heat loss from the receiver walls. Moreover, the flow condition at the inlet was considered a fully developed flow. A comprehensive approach was adopted to verify the accuracy of the FV model. Typical results of the simulation are presented. A finite volume based software package, ANSYS Fluent 15.0 [23], was used for this modelling and simulation.

2 Physical Model

The LS2 PTC was used in the Solar Energy-Generating System (SEGS) III–VII 150 MW plants, Kramer Junction, California, USA, which is a proven solar collector for solar thermal electricity generation [9]. The geometric configuration of the collector and the receiver are shown in Figs. 2 and 3, respectively. The mirror aperture is 5×7.8 m^2, and the receiver tube is 8 m long with 66 mm inner diameter and 2 mm wall thickness. In order to increase the flow velocity of the HTF, Dudley et al. [9] inserted a 50.8 mm diameter closed-end plug inside the receiver tube. The HTF was Syltherm800 silicone based oil. The LS2 collector module was tested on the AZTRAK rotating platform at Sandia National Laboratory (SNL) by Dudley et al. [9]. Thermal energy performances of the collector under three physical conditions relating to the glass envelope of the receiver: (i) the glass envelope was evacuated, (ii) lost vacuum or air inside the envelope and (iii) removed glass cover or bare receiver was investigated. As has been mentioned earlier, since, the glass cover has direct contact with the Photovoltaic (PV) solar cells of a CPV/T collector; the convection loss, along with the radiation loss, must
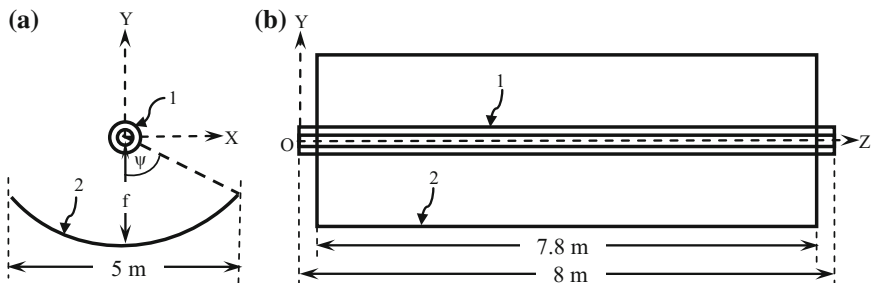

Fig. 2 Schematic of the LS2 collector on Cartesian coordinate system: **a** cross-sectional view on XY plane, and **b** top view on XZ plane (In the figure, the numerals 1 and 2 refer the evacuated receiver and the parabolic mirror, respectively, f is the focal length (=1.84 m), and ψ is the rim angle of the mirror ($\approx 70°$))
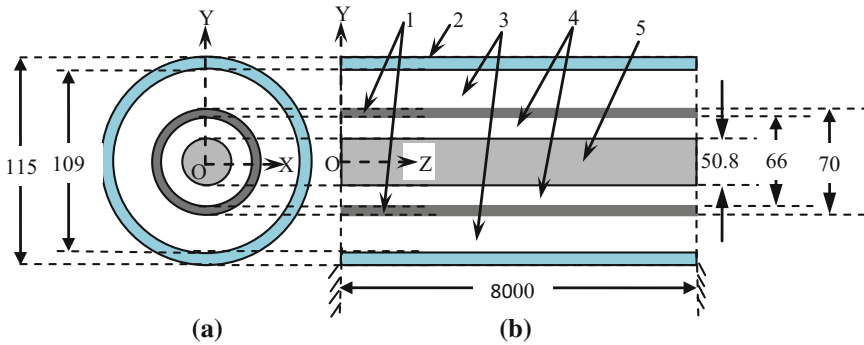
Fig. 3 Geometry of the LS2 collector receiver: **a** Cross-sectional view on XY plane, and **b** longitudinal section of the receiver on YZ plane (In the figure, the numerals 1, 2, 3, 4 and 5 refer to the absorber tube, glass tube, evacuated passage between the glass tube and the absorber tube, heat transfer fluid passage and the flow restriction device, respectively. All dimensions are in mm)
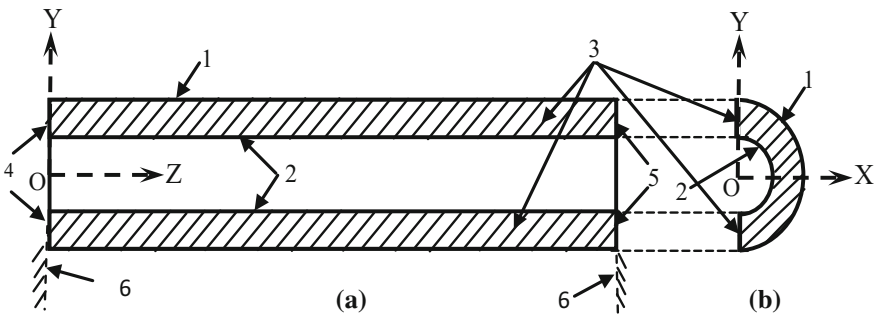

Fig. 4 Heat transfer fluid (HTF) domain of the receiver for the finite volume (FV) model on the OXYZ coordinate system, and the boundary conditions: **a** longitudinal section of the domain on YZ plane, and **b** the angular cross-section on XY plane (In the figure, the numerals 2, 3, 4, 5 and 6 refer to no-slip heat flux wall, no-slip adiabatic inside wall, symmetry, fully developed velocity inlet, fully developed pressure outlet, and adiabatic ends of the receiver, respectively)

take place from the PV surface to the environment. Therefore, to account for this environmental effect on the CPV/T collector receiver, the bare receiver of the LS2 collector was modelled for the current finite volume simulation so that the heat losses could be simulated and verified.

The irradiance distribution along the periphery of the receiver tube of the LS2 collector under ideal conditions, applying the MCRT optical simulation technique was found perfectly symmetric to the plane of geometric symmetry of the collector (YZ plane in Fig. 2). Therefore, the HTF domain of right-hand-side half of YZ plane was modelled as shown in Fig. 4 so as to minimize the computational expense utilizing of the characteristics of physical symmetry. The flow restriction device and the metal tube were not modelled for this conjugate heat transfer analysis as the flow properties were assumed steady state. Therefore, the shape of

the computational domain was semi-cylindrical and horizontal. Gravity was acting vertically downward along the Y-axis. Several test conditions with the bare receiver of the collector as presented in Table 1 were selected for the current simulation.

3   Computational Model Development

3.1   *Governing Equations*

As the minimum Reynolds number (Re) was more than 6000, the flow criteria of the selected test conditions as shown in Table 1 were turbulent considering the critical Reynolds number, Re_c 4000; incompressible; and steady state [9]. The turbulent energy production, κ, and the turbulent energy dissipation, ε, were calculated using the RNG $\kappa-\varepsilon$ transport equations. The governing equations and the transport equations were as given below:

The mass conservation equation or the continuity equation can be expressed in differential form as.

The mass continuity equation could be simplified as a volume continuity equation for Syltherm800 oil at steady state condition as:

$$\nabla \bullet u_i = \frac{\partial u}{\partial x} + \frac{\partial v}{\partial y} + \frac{\partial w}{\partial z} = 0 \tag{1}$$

Considering the gravity along the global $-y$ direction, the momentum equations for a Three-Dimensional (3D) steady state incompressible flow can be rewritten as

$$\rho(u\frac{\partial u}{\partial x} + v\frac{\partial u}{\partial y} + w\frac{\partial u}{\partial z}) = -\frac{\partial p}{\partial x} + (\mu + \mu_t)\left\{\frac{\partial^2 u}{\partial x^2} + \frac{\partial^2 u}{\partial y^2} + \frac{\partial^2 u}{\partial z^2}\right\} \tag{2}$$

$$\rho(u\frac{\partial v}{\partial x} + v\frac{\partial v}{\partial y} + w\frac{\partial v}{\partial z}) = -\frac{\partial p}{\partial y} + (\mu + \mu_t)\left\{\frac{\partial^2 v}{\partial x^2} + \frac{\partial^2 v}{\partial y^2} + \frac{\partial^2 v}{\partial z^2}\right\} - \rho g_y \tag{3}$$

Table 1 Selected test conditions of the bare receiver of the LS2 collector from Dudley et al. [9]

Test conditions	DNI (W/m^2)	T_{amb} (°C)	T_{in} (°C)	V_{HTF} (m/s)	Re	T_{out} (°C)	V_{air} (m/s)
1st	919	22.6	301.4	0.608,157	12,710.1	318	0.1
2nd	867.6	19.8	203.4	0.597,403	6431.098	219.6	0.5
3rd	929.8	21.8	252.2	0.606,962	9218.136	269	1
4th	941.1	13.5	313.1	0.667,897	14,950.33	322	8
5th	961.3	15.1	313.3	0.667,897	14,967.46	320.7	9.3

DNI daily normal insolation, *T* temperature, *V* velocity, *Re* Reynolds number, *HTF* heat transfer fluid, *amb* ambient, *in* inlet, and *out* outlet

$$\rho(u\frac{\partial w}{\partial x}+v\frac{\partial w}{\partial y}+w\frac{\partial w}{\partial z})=-\frac{\partial p}{\partial z}+(\mu+\mu_t)\left\{\frac{\partial^2 w}{\partial x^2}+\frac{\partial^2 w}{\partial y^2}+\frac{\partial^2 w}{\partial z^2}\right\} \quad (4)$$

where, μ and μ_t were the molecular viscosity and turbulent (eddy) viscosity, respectively.

The conservation of energy equation was based on the energy balance that can be computed by the formula

$$\rho c_p\frac{\partial T}{\partial t}+\rho c_p\nabla.(u_iT)=-\nabla p+\left[k+\frac{c_p\mu_t}{\mathrm{Pr}_t}\right]\nabla^2 T+(\mu+\mu_t)\frac{\partial u_i}{\partial x_j}\left\{\frac{\partial u_i}{\partial x_j}+\frac{\partial u_j}{\partial x_i}-\frac{2}{3}\frac{\partial u_k}{\partial x_k}\delta_{ij}\right\}+S_r \tag{5}$$

where, S_r is solar radiation source term.

Two transport equations for RNG $\kappa\text{-}\varepsilon$ model to calculate the turbulent energy production, κ and the turbulent energy dissipation, ε were

$$\frac{\partial}{\partial t}(\rho\kappa)+\nabla.(\rho\kappa u_i)=\alpha_\kappa(\mu+\mu_t)\nabla^2\kappa+G_\kappa+G_b-\rho\varepsilon \tag{6}$$

$$\frac{\partial}{\partial t}(\rho\varepsilon)+\nabla.(\rho\varepsilon u_i)=\alpha_\varepsilon(\mu+\mu_t)\nabla^2\varepsilon+C_{1\varepsilon}\frac{\varepsilon}{\kappa}(G_\kappa+C_{3\varepsilon}G_b)-\rho C_{2\varepsilon}^*\frac{\varepsilon^2}{\kappa} \tag{7}$$

,respectively.

Where, $C_{1\varepsilon}$ and $C_{3\varepsilon}$ were two model constants equal to 1.42 and 1.68, respectively, G_κ and G_b were turbulent kinetic energy generation due to mean velocity gradient and buoyancy effect, respectively, and α_κ and α_ε were the inverse effective Prandtl numbers for κ and ε, respectively.

Eddy viscosity was modified for swirl generation in the RNG model as

$$\mu_t=\rho C_\mu\frac{\kappa}{\varepsilon}f(\alpha_s,\Omega,\frac{\kappa}{\varepsilon})-\rho C_{2\varepsilon}^*\frac{\varepsilon^2}{\kappa} \tag{8}$$

Table 2 Temperature (K)-dependent correlations for the HTF physical properties

Properties	$=a+bT+cT^2+dT^3+eT^4+\text{———}$					Temperature range (K)
	a	b	c	d	e	
$\rho(\text{kg/m}^3)$	1139.2	−0.546	−4.87e−04			233 to 673
$c_p(\text{J/kg K})$	1108.2	1.7073				233 to 673
k (W/m K)	0.1901	−1.88e−04				233 to 673
μ (Pa S)	0.2591	−8.93e−04				233 to 273
	0.157	−8.00e−04	1.03e−06			273 to 340
	0.0848	−5.54e−04	1.39e−06	−1.57e−09	6.67e−13	340 to 673
$k_{\text{Steel}}=15.906+0.0025T^2+5\text{e-}05T^3$ W/mK						
ρ Density, c_p isobaric heat capacitance, k thermal conductivity, μ dynamic viscosity						

where, $C_\mu = 0.0845$, α_s was the swirl constant roughly set to 0.07 for mild swirl flows and even higher value can be set for a strong swirl flow, and Ω was a characteristics swirl number that was calculated inside the ANSYS Fluent.

3.2 Physical Properties of the Computational Domain

The constituent of the computational domain as shown in Fig. 4 was the Syltherm 800 fluid. The physical properties including the density, isobaric heat capacitance, thermal conductivity and the dynamic viscosity of the HTF were correlated with its instantaneous absolute temperature. The polynomial correlations were developed as given in Table 2. The tube material, which was not modelled, was steel, and the thermal conductivity of steel, k_{Steel}, was also correlated with its absolute temperature as included in the same table.

3.3 Assumptions and the Boundary Conditions of the Computational Domain

As Fig. 4 shows, the boundary conditions in the computational domain were: **1:** no-slip heat flux wall, **2:** no-slip adiabatic wall, **3:** symmetry, **4:** fully developed velocity inlet and pressure outlet, and **5:** adiabatic ends of the receiver. They are explained in details below.

1. **The no-slip heat flux wall**: The inside surface and the outside surface of the absorber tube formed this no-slip heat flux boundary wall of the computational domain. The outside surface of the tube was exposed directly to the concentrated solar radiation and the environment; and the inside one was in direct contact with the viscous, pressurized and incompressible HTF. Shell conduction in the wall was active.

The outside surface of the tube was absorbing the incident solar irradiation energy as heat flux, and the inside surface was losing the heat energy to the flowing HTF. Simultaneously, because of the environmental effect, the outside surface was also losing some of the heat energy due to the radiation and convection heat losses. The rate of the concentrated solar energy and its density distribution around the receiver tube was calculated by applying the MCRT technique, which was coupled with the current FV model applying a special coupling technique as discussed in Sect. 3.4. The theoretical framework and the calculation technique of the heat loss from the outside surface of the tube are described in Sect. 3.5.

On the other hand, the convective and the conductive energy transfer from the inside surface of the tube to the HTF were calculated applying the built-in finite volume technique of the ANSYS Fluent software package. Moreover, the inside surface of the tube was assumed sufficiently frictional to form a no-slip wall to the viscous HTF.

2. **The no-slip adiabatic wall**: The circumferential surface of the cylindrical flow restriction device that was immersed into the viscous, pressurized and incompressible HTF as shown in Fig. 3 formed this wall boundary condition. The surface of the devise was assumed sufficiently frictional to the HTF to form a no-slip boundary. On the other hand, at steady state condition, no energy exchange between the device and the HTF was assumed.

As the RNG κ-ε turbulence model was not that efficient in calculation of the flow parameters near the wall, standard wall functions developed by Launder and Spalding [24] were used for near wall treatment. The logarithmic law-of-the-wall for mean velocity is given by the following formula:

$$U^* = \frac{\ln(Ey^*)}{\kappa} \tag{9}$$

where, $U^* \equiv \left(U_P C_\mu^{0.25} K_P^{0.25} \right) / (\tau_w/\rho)$, $y^* \equiv \left(\rho C_\mu^{0.25} K_P^{0.25} y_P \right)/\mu$, κ = von Kármán constant (= 0.4187), E = empirical constant (= 9.793), U_P = mean velocity of the fluid at point P, K_P = turbulence kinetic energy at point P, y_P = distance from point P to the wall, and μ = dynamic viscosity of the fluid.

This law is only valid for y^* between 30 and 300. In Fluent, the log-law is employed when y^* of the mesh adjacent to the wall is larger than 11.225. But the laminar stress-strain relationship, $U^* = y^*$ is used for the values smaller than 11.225. The laws-of-the-wall for mean velocity and temperature are based on the wall unit, y^*, rather than y^+ ($\equiv \rho u_\tau y/\mu$). However, these quantities are approximately equal in equilibrium turbulent boundary layers.

3. **Symmetry**: The shape of the HTF domain in between the absorber tube and the flow restriction device was annular or hollow cylindrical. The thickness of the annulus was assumed to be perfectly uniform. Moreover, the incident concentrated light around the external surface of the annulus was found symmetric either side of the YZ plane (see Fig. 3) along the periphery. The HTF flow inside the annulus was assumed symmetric with respect to the YZ plane. Therefore, the flow criteria and the conjugate heat transfer characteristics were assumed symmetric to the YZ plane.

4. **Fully developed velocity inlet and pressure outlet**: As the HTF inlet of the computational domain of the modelled receiver was downstream of a sufficiently long close-channel flow line, the flow of Syltherm800 viscous oil inside the no-slip annulus at the inlet must be fully developed turbulent flow. The flow was simulated as fully developed flow instead of assuming simplistic average fluid velocity such that [25]:

$$\frac{\partial u_i}{\partial z} = \frac{\partial k}{\partial z} = \frac{\partial \varepsilon}{\partial z} = \frac{\partial p}{\partial z} = \frac{\partial T}{\partial z} = 0 \tag{10}$$

5. **Adiabatic edges**: The rest of the HTF flow line except the computational domain enclosed within the HTF inlet and outlet was assumed perfectly insulated, therefore, no or negligible heat losses were assumed from inlet and outlet edges of the domain. Moreover, the bracket loss at the steady state condition was also assumed negligible.

3.4   Coupling Between MCRT and FV Models

As explained in Sect. 3.3, the no-slip heat flux boundary wall was absorbing the concentrated light that was reflected from the parabolic trough mirror. The distribution of the irradiance along the periphery of the computational domains of the both the receiver elements was calculated using a well verified MCRT model. The irradiance distribution around the receiver was calculated as Local Concentration Ratio (LCR). The integration between the MCRT and the FV models in the literature could be found sharing the same local irradiance data table by the models [17, 25, 26] provided that the grid at the outer surfaces of the physical model was the same, and the analysis of the optical and thermal behaviour of the collector were simultaneous and dependent. On the contrary, a unique approach for the current FV model was adopted in which both models shared the same irradiance profile yet they were completely independent in their grid system and analysis.

Predicting the LCR profiles of the LS2 receiver for a large number of test conditions, two sets of polynomial correlations were developed applying the curve fitting technique as a function of angular location, β (°) of the receiver. Using the correlations, the local irradiance around the receiver with evacuated glass envelope and without glass envelope could be calculated. The correlations with their coefficients of determination, R^2, were given by the following set of equations for the receiver with glass envelope:

$$
\begin{aligned}
I_{0° \leq \beta \leq 15°} &= C_1 \times (2.8e - 3 \times \beta^3 - 1.29e - 2 \times \beta^2 + 0.1333 \times \beta + 43.333), (R^2 = 0.9973) \\
I_{15° < \beta \leq 48°} &= C_1 \times (6.98e - 3 \times \beta^2 - 0.108 \times \beta + 52.414), (R^2 = 0.9988) \\
I_{48° < \beta \leq 90°} &= C_1 \times (1.2849e - 3 \times \beta^3 - 0.2622 \times \beta^2 + 15.74 \times \beta - 229.49), (R^2 = 0.9999) \\
I_{90° < \beta \leq 180°} &= C_1 \times (-1.06e - 4 \times \beta^2 + 4.24e - 2 \times \beta - 2.9507), (R^2 = 0.9973)
\end{aligned}
\tag{11}
$$

and without glass envelope:

$$
\begin{aligned}
I_{0° \leq \beta \leq 15°} &= C_2 \times (1.98e - 4 \times \beta^4 - 3e - 3 \times \beta^3 + 2.37e - 2 \times \beta^2 + 3.59e - 2 \times \beta + 46.453), (R^2 = 0.9857) \\
I_{15° < \beta \leq 48°} &= C_2 \times (1.19e - 4 \times \beta^3 - 4.1e - 3 \times \beta^2 + 0.2074 \times \beta + 49.602), (R^2 = 0.997) \\
I_{48° < \beta \leq 90°} &= C_2 \times (1.230434e - 3 \times \beta^3 - 0.2511 \times \beta^2 + 15.012 \times \beta - 214.19), (R^2 = 0.9999) \\
I_{90° < \beta \leq 180°} &= C_2 \times (-1.055e - 4 \times \beta^2 + 4.19e - 2 \times \beta - 2.9121), (R^2 = 0.9954)
\end{aligned}
$$

$$\tag{12}$$

Fig. 5 Calculation of the irradiance distribution along the circumference of the computational domain using the set of correlations of Eq. (12)
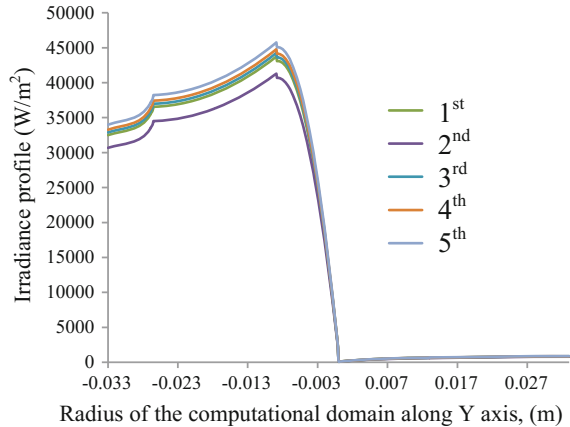
where, $C_1 = DNI \times \rho_{PT} \times \tau_{GT} \times \alpha_{RT}$, $C_2 = DNI \times \rho_{PT} \times \alpha_{RT}$, R^2 = Coefficient of determination and DNI = Daily normal insolation (W/m^2).

The irradiance distributions along the circumference of the computational domain for the selected test conditions as presented in Table 1 were calculated using the set of correlations (12) as shown in Fig. 5. As the DNI for the most of the test conditions were very close, the irradiance profiles were also found very close to each other.

Incorporating the correlations, an in-house subroutine was developed by using the ANSYS macros, which was interpreted in the FV model. The solar energy in the macro was treated as heat flux and surface phenomenon of the domain. The irradiance profile was assumed uniform along the tube length. At the inlet and outlet, each edges of the receiver tube were larger than the mirror by 100 mm, therefore, was shaded (see Fig. 2). The macro enabled a grid independent coupling between the MCRT and the FV model. The heat loss from the outside wall of the domain to the environment by means of radiation and convection was also incorporated in the same macro applying the following theories.

3.5 The Radiation and Convection Heat Losses from the Outside Surface

As the absorber tube was bare, both the radiation and convection heat losses from the wall to the ambient were considered as surface phenomena. The following algorithm for the heat loss calculation was incorporated into the same MCRT-FV coupling macro.

The radiation heat loss was calculated by the formula

$$q_{rad} = \varepsilon\sigma[F_{gr}(T_w^4 - T_{gr}^4) + F_{sky}(T_w^4 - T_{sky}^4)] \tag{13}$$

where, ε was the emissivity of the cermet coated absorber tube that was given by, $\varepsilon = 0.000327T_w - 0.065971$ [10], σ was the Stefan–Boltzmann constant ($= 5.670373 \times 10^{-8}$ W/m²K⁴), F was the radiation view factor, and T was temperature in Kelvin. The subscripts 'gr', 'w' and 'sky' referred to the ground, wall and the sky, respectively.

The view factor between the receiver and the ground, F_{gr}, and between the receiver and the sky, F_{sky}, were calculated respectively, as:

$$\begin{aligned} F_{gr} &= 0.5(1 + \cos\beta) \\ F_{sky} &= 0.5(1 - \cos\beta) \end{aligned} \tag{14}$$

where, β was the angular location on the receiver in OXY plane such that $\beta = 0°$ along $-$OY axis and 180° along $+$OY axis (see Fig. 4).

The ground temperature, $T_{gr} = T_a$, whereas, the sky temperature, $T_{sky} = T_a - 8$ [10]. Here, the subscript 'a' refers to the air or ambient.

On the other hand, as the selected test conditions in Table 1 shows wind speed during the data collection, forced convection heat loss from the receiver surface was assumed. The loss per unit surface area was given by:

$$q_{convec} = h(T_w - T_a) \tag{15}$$

where, h was the forced convection coefficient. As the exact event was not known, h was calculated as average of leeward coefficient, h_{lee} and wind-ward coefficient, h_{wind}. According to Sharples and Charlesworth [27], these coefficients were calculated by,

$$\begin{aligned} h_{lee} &= 2.2V_a + 8.3 \\ h_{wind} &= 3.3V_a + 6.5 \end{aligned} \tag{16}$$

where, V was the velocity of air.

3.6 Grid Generation Technique for the Computational Domain of LS2 Receiver

The accuracy and the stability of numerical simulation strongly rely on the grid resolution and distribution inside the computational domain. The mesh resolution should be fine enough, and the distribution should be reasonable to some regions of the domain in order to capture the flow physics properly; otherwise, an exaggerated
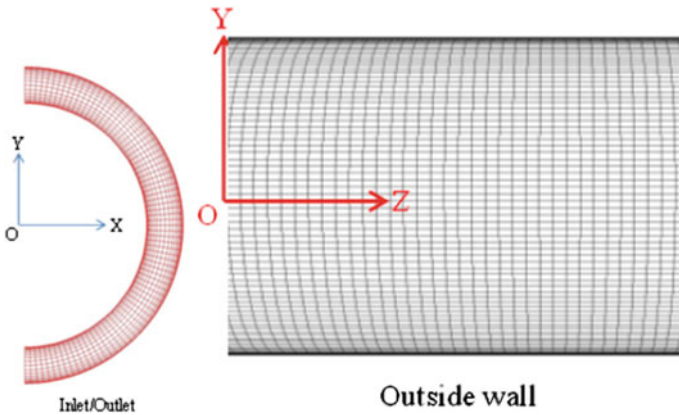
Fig. 6 Grid structure distribution for the computational domain

result would be produced from the simulation. As the current computational simulation involves turbulent flow along the Z axis, and high-temperature heat transfer across the XY plane from the wall to the viscous HTF, the grid resolution near the wall must be fine enough in order to capture the flow physics, that is, the viscous and thermal boundary layers near the frictional wall; and the grid must be distributed such a way that the effect of viscosity and heat transfer by means of convection (diffusion and advection) across the flow is resolved. Therefore, a structured and hexahedral grid system was generated for the current computational domain in such a way that the grids were uniformly distributed along the HTF flow (see the grid system on the YZ plane at the Outside wall, and along the Z axis at the symmetry in Fig. 6) and inflated by 10% across the flow from the wall to the centre of the bulk flow (see the grid system on the XY plane at the Inlet/Outlet face, and along the Y-axis at the Symmetry in Fig. 6). However, the optimum grid resolution was decided by performing the grid independence test as explained in Sect. 4.1.

3.7 Solution Method

The governing equations describing the current conjugate heat transfer fluid flow model were highly nonlinear and coupled in nature that made them almost impossible to obtain an analytical solution applying by available knowledge. Instead, an approximate numerical solution would be an efficient technique for this kind of real world problem. However, the accuracy and/or the acceptability of the solution to the experts simply rely on the adopted numerical scheme and the solution method.

The FV method was adopted for the current simulation to discretise the governing equations. The discretization was facilitated by employing one of the highly reliable FV based CFD software packages, ANSYS Fluent 14.5.

As the shell conduction within the material of the receiver was accounted for in the simulation, a segregated numerical method was selected between the segregated and coupled (implicit and explicit)—two available solution methods in ANSYS Fluent. Using this approach, the governing equations were solved sequentially, that is, segregated from one another. As the governing equations are nonlinear and coupled, several iterations of the solution loop must be performed before a converged solution is obtained. Any iteration consists of the steps as outlined below:

1. Fluid properties are updated, based on the initialized solution at the first iteration, and based on the current solution at the subsequent iteration.
2. In order to update the velocity field, the u, v, and w momentum equations are each solved in turn using current values for pressure and face mass fluxes.
3. Since the velocities obtained in Step 2 may not satisfy the continuity equation locally, a 'Poisson-type' equation for the pressure correction is derived from the continuity equation and the linearized momentum equations. This pressure correction equation is then solved to obtain the necessary corrections to the pressure and velocity fields and the face mass fluxes such that continuity is satisfied.
4. Where appropriate, equations for scalars such as turbulence, energy, and species are solved using the previously updated values of the other variables.
5. When interphase coupling is to be included, the source terms in the appropriate continuous phase equations may be updated with a discrete phase trajectory calculation.
6. A check for convergence of the equation set is made.
7. These steps are continued until the convergence criteria are met.

As the grid system of the current computational domain was hexahedron, and the upstream and the downstream of the domain were fully specified; in order to achieve a better accuracy in the simulation, a higher order Quadratic upwind differencing scheme: the QUICK scheme [28, 29] was adopted to discretise 3D convection-diffusion problem. Quick type schemes are based on a weighted average of second-order upwind and central interpolations of the variable. However, undertaking calculations with a higher order differencing scheme like QUICK sometimes would experience an instability problem in the solution because of some reason like poor initial guess. In order to minimize this chance of instability, after the initialization of the solution, the calculation was accomplished in three different steps: (1) first 50 to 500 iterations with first order upwind scheme, (2) next 50 to 500 more iterations with the second-order upwind scheme, and (3) finally resume the calculation until convergence of the solution activating the QUICK scheme. Because of the inherent limitations of the standard, linear, second-order and

body-force-weighted pressure interpolating schemes, the PRESTO! scheme was adopted for the current simulation as this particular scheme is applicable with all types of grid systems. In FLUENT, SIMPLE is the default pressure-velocity coupling technique. Therefore, the SIMPLE algorithm was selected for the current steady state and turbulent HTF flow model. In the present study, the under-relaxation factors were set as 0.3 for the pressure and momentum, 0.8 for turbulent dissipation rate, and 0.75 for the rest of the parameters. The maximum allowable residuals were set at 10^{-6} for the energy equation, and 10^{-4} for the rest of the parameters. However, at the end of the computations of the present FV model, the residuals of the most of the values were found to be a couple of order less than the set values.

4 Verification of the Model

4.1 Grid Independence Test to Decide the Optimum Grid Resolution

In Sect. 3.6, a grid generation technique for the computational domain of the LS2 receiver element was illustrated. In this section, how the optimum grid system for the receiver element was adopted is explained.

The grid independence test is an approximate measure of whether the grid system in a computational domain is optimally fine; otherwise, the simulation result might be misleading. As the present FV model was a conjugate heat transfer simulation of steady state turbulent flow, the HTF temperature near the outlet of the domain was presumed to be the highest within the domain. Therefore, the optimum grid resolution was decided based on the effect of grid resolution on the static temperatures at two different locations on the heat flux wall (see Sect. 3.3) and the adiabatic wall (see Sect. 3.3) close to the HTF outlet. Nine different grid systems were generated, and the static temperature near the HTF outlet at two points on the inside and outside walls of the domain were calculated as shown in Fig. 7. As the figure shows, analysing the variations in the recorded temperatures, the grid system $20_r \times 60_\beta \times 1600_z$ was found satisfactory for the current computational domain. Here, suffix r, β and z refer to the radial, angular/circumferential and axial direction of the domain. However, for further accuracy and to get maximum benefit of high-performance computing (HPC) facilities at the Queensland University of Technology (QUT) the grid system $20_r \times 80_\beta \times 3200_z$ was chosen for the current model that produced 5,120,000 hexahedral cells.

Fig. 7 Grid independence
test
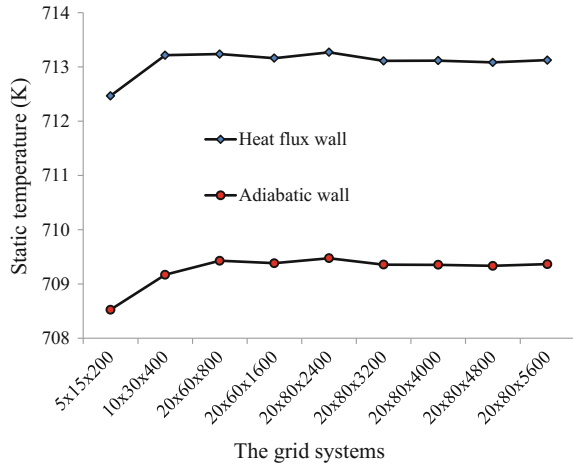
4.2 Checking the Near Wall Grid Resolution

The value of wall Y* and/or Y+ is an indication of whether the grid resolutions near the wall are fine enough, or the first cell adjacent to the wall is within the boundary layer so that the flow physics inside the computational domain near the no-slip wall is resolved properly. Lower values of Y* and the Y+ correspond to a fine mesh near the wall. Therefore, Y* and Y+ of both of the walls (the heat flux wall and the adiabatic wall) of the computational domain were calculated from the FV model as shown in Figs. 8 and 9, respectively. The figures show that the maximum Y* value was 4.16, and the maximum Y + value was 4.19 on the outside wall near the HTF outlet where the temperature was maximum. As the maximum Y* value was lower than 11.225, the laminar stress-strain relationship was employed in calculation of this value (see the Sect. 3.3). The minimum values of Y* and Y+ were calculated 2.76 and 2.78, respectively, which were also could be found on the outside wall near the inlet edge where the temperature was minimum relative to the entire domain. That implies that the near wall grid resolution was fine enough.

4.3 Verification of the FV Model and the MCRT-FV Integration

The current FV model was used to calculate the HTF outlet temperature for five different test conditions for the bare receiver of LS2 collector. The outlet temperatures HTF of the simulated test conditions were compared with the experimental results as presented in Table 3. The maximum absolute error between the simulated
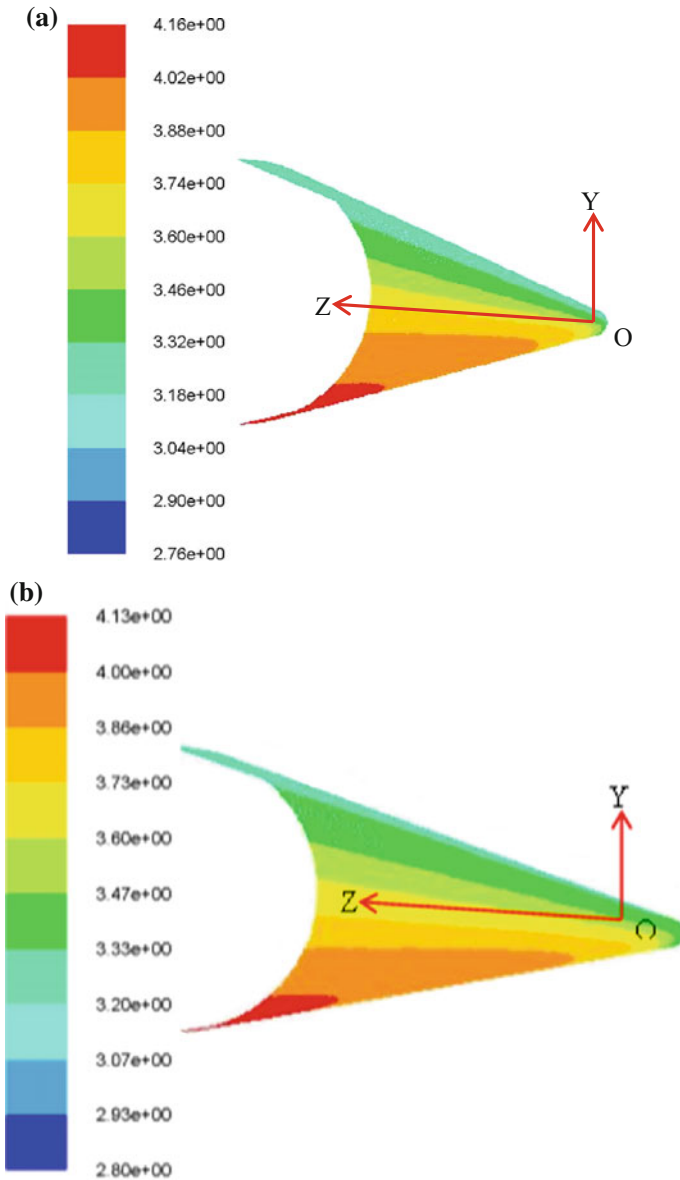
Fig. 8 Wall Y* values: **a** at outside wall, and **b** at inside wall

results and the experimental results were calculated to be 2.92% for the second test condition, and the minimum absolute error was calculated to be 0.23% for the fourth test condition. The average absolute error was calculated to be 1.11%. This
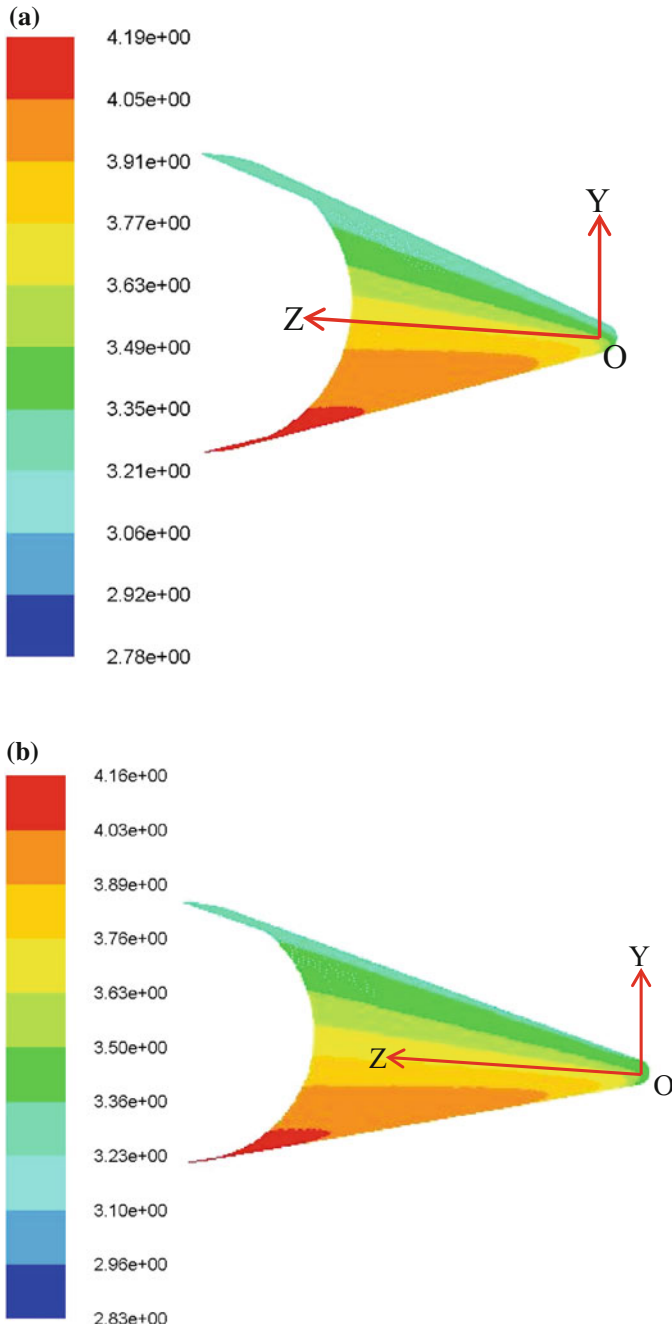
(a)

4.19e+00
4.05e+00
3.91e+00
3.77e+00
3.63e+00
3.49e+00
3.35e+00
3.21e+00
3.06e+00
2.92e+00
2.78e+00

(b)

4.16e+00
4.03e+00
3.89e+00
3.76e+00
3.63e+00
3.50e+00
3.36e+00
3.23e+00
3.10e+00
2.96e+00
2.83e+00

Fig. 9 Wall Y+ values: **a** at outside wall, and **b** at inside wall

Table 3 Comparison of model calculated results with experimental data

TCs	DNI (W/m^2)	V$_a$ (m/s)	T$_a$ (°C)	T$_{in}$ (°C)	T$_{o\_expt}$ (°C)	T$_{o\_model}$ (°C)	E$_{abs}$ (%)	E$_{av}$ (%)
1st	919	0.1	22.6	301.4	318	320.98	0.94	1.11
2nd	867.6	0.5	19.8	203.4	219.6	213.19	2.92	
3rd	929.8	1	21.8	252.2	269	271.68	1.04	
4th	941.1	8	13.5	313.1	322	322.73	0.23	
5th	961.3	9.3	15.1	313.3	320.7	322.08	0.43	

Acronyms: *TC* Test Conditions, *DNI* Daily Normal Insolation, *V* Velocity, *T* Temperature, *E* Error. Suffixes: *a* air or ambient, *in* inlet, *o_expt* experimental outlet data, *o_model* model calculated outlet data, *abs* absolute, *av* average

Table 4 Comparison of outlet temperature at different heat loss conditions

Test conditions	V$_a$ (m/s)	T$_i$ (°C)	No loss model	Total loss model			Convection loss model		Radiation loss model	
			T$_{o\_Max}$ (°C)	T$_{o\_Min}$ (°C)	q$_{loss\_Max}$ (%)	T$_{o\_Convec}$ (°C)	q$_{loss\_Convec}$ (%)	T$_{o\_Rad}$ (°C)	q$_{loss\_Rad}$ (%)
1st	0.1	301.4	325.45	320.98	18.60	322.20	13.52	324.18	5.30
2nd	0.5	203.4	215.90	213.19	21.64	213.57	18.65	215.51	3.11
3rd	1	252.2	275.94	271.68	17.91	272.21	15.69	274.94	4.21
4th	8	313.1	335.74	322.73	57.47	323.85	52.54	334.43	5.80
5th	9.3	313.3	336.43	322.08	62.05	323.18	57.28	335.11	5.71

In the table, *V* is velocity, *T* is temperature and *q* is heat energy per second. Suffix *a, i, o, Max, Min, Convec* and *Rad* stand for air, inlet, outlet, maximum, minimum, convection and radiation, respectively

good agreement between the simulated results and the experimental results was validated the accuracy of the current FV model and the MCRT-FV integration macro.

4.4 Verification of the Heat Loss Calculation Algorithm

As the receiver was bare, ambient conditions strongly affected the convection and radiation heat losses from the surface of the computational domain. The loss was calculated using an in-house subroutine coupled with the MCRT-FV integration macro. The test conditions were simulated assuming four different heat loss conditions including, (i) no loss model, (ii) total loss model, (iii) convection loss model, and (iv) radiation loss model. The estimated HTF outlet temperature and the percentage of heat loss data were arranged in Table 4. One might understand from the general knowledge of heat transfer that the HTF outlet temperature would be the maximum without heat loss, the minimum with total loss (both convection and

radiation heat losses), and in between these maximum and minimum temperatures with the convection heat loss and the radiation heat loss. The calculated outlet temperatures of the HTF under all four heat loss conditions as presented in the table support the general knowledge completely. This particular investigation confirmed the reliability of the heat loss algorithm that used in the in-house macro with the MCRT-FV integration macro.

4.5 Checking the Fully Developed Flow Condition at the HTF Inlet

As discussed in Sect. 3.3, the HTF flow at the inlet was considered fully developed instead of average bulk flow. Firstly, in case of the average velocity assumption, the longitudinal velocity (the Z velocity for the current models) across the flow (from the wall to the bulk flow centre) is uniform and becoming fully developed along the downstream gradually or rapidly depending on the turbulence. Whereas, in case of the fully developed flow, the longitudinal velocity is zero adjacent to the wall due to a viscous share effect and developed fully at the bulk flow centre of the HTF where all of the flow properties are in steady state condition according to Eq. (10). Secondly, the velocity components perpendicular to the bulk flow (the X and Y velocities for the current models) are zero in case of average or uniform velocity assumption, whereas, the components are nonzero at fully developed flow. Finally, the longitudinal or bulk flow velocity contours of a steady state flow at the inlet and outlet of a solved computational domain would be exactly similar to each other if the flow is isothermal and adiabatic; otherwise, would be fairly similar. The velocity contours at the HTF inlet, outlet and symmetry boundaries of the computational domains of both of the receiver elements were visually investigated and compared against these three criteria for the flow to be fully developed at the inlet.

The velocity contours at the HTF inlet and outlet boundaries of the computational domain of the LS2 receiver are shown in Figs. 10 and 11, respectively. The longitudinal velocity profile and the Z velocity contour in Fig. 10c match perfectly with the first criterion as the velocity near the wall is zero, and maximum at the centre. Moreover, the velocity components perpendicular to the axial velocity, the X velocity and the Y velocity in Fig. 10a and b, respectively, match perfectly with the second criteria as none of these components are nonzero. Finally, the axial velocity contour at the inlet (see Fig. 10c) could be seen to match perfectly with that at the outlet (see Fig. 11c). However, the dissimilarities, if any, could be seen by visual investigation between the velocity contours of X, Y and Z velocity components at the inlet (see Fig. 10) and those components at the outlet
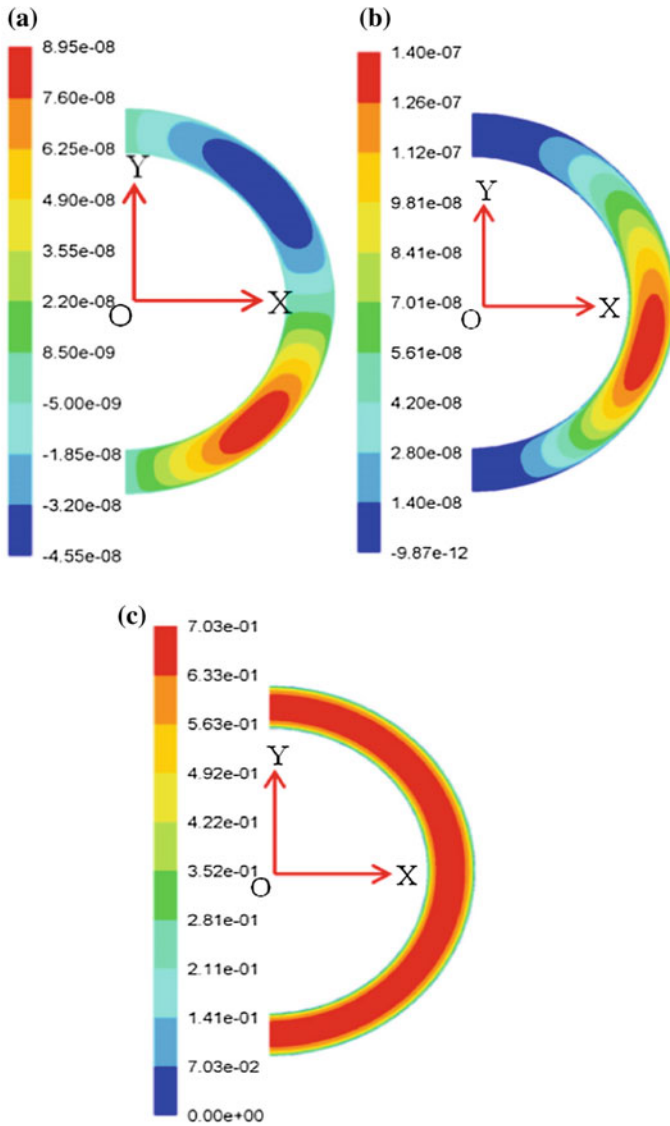
Fig. 10 Velocity contour at the inlet: **a** X velocity, **b** Y velocity and **c** Z velocity

(see Fig. 11) were might be because of conjugate heat transfer effect across the flow. Nonetheless, it could be claimed that the simulation of the fully developed flow at the HTF inlet of the computational domain of the LS2 receiver was appropriate.
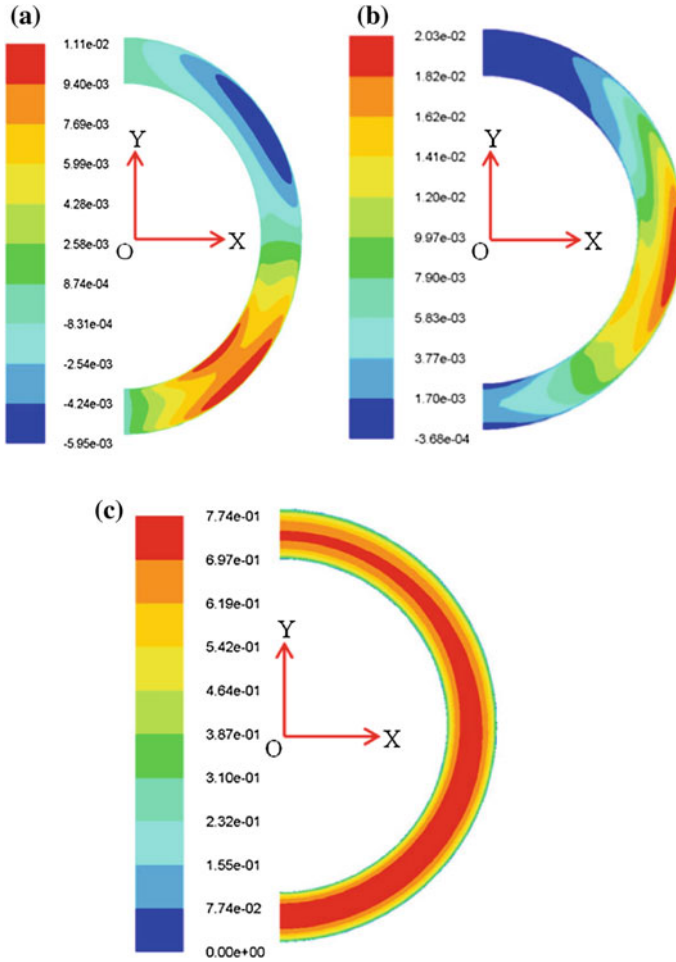
Fig. 11 Velocity contour at the outlet: **a** X velocity, **b** Y velocity and **c** Z velocity

4.6 Further Verification of the MCRT-FV Integration

The accuracy of MCRT-FV integration was already justified in Sect. 4.3. However, the integration is further verified comparing the residual heat flux profile around the circumference of the computational domain as shown in Fig. 12a. The purpose of the integration was to reproduce a realistic and appropriate concentrated solar energy flux profile around the circumference of the computational domain as shown in Fig. 5. Whether the algorithm and the employed macro for the integration worked properly could be justified comparing the similarity between the input concentrated solar flux profile as shown in Fig. 5 with the residual wall heat flux profile in Fig. 12a. However, the magnitude of the solar flux in Fig. 5 could be seen
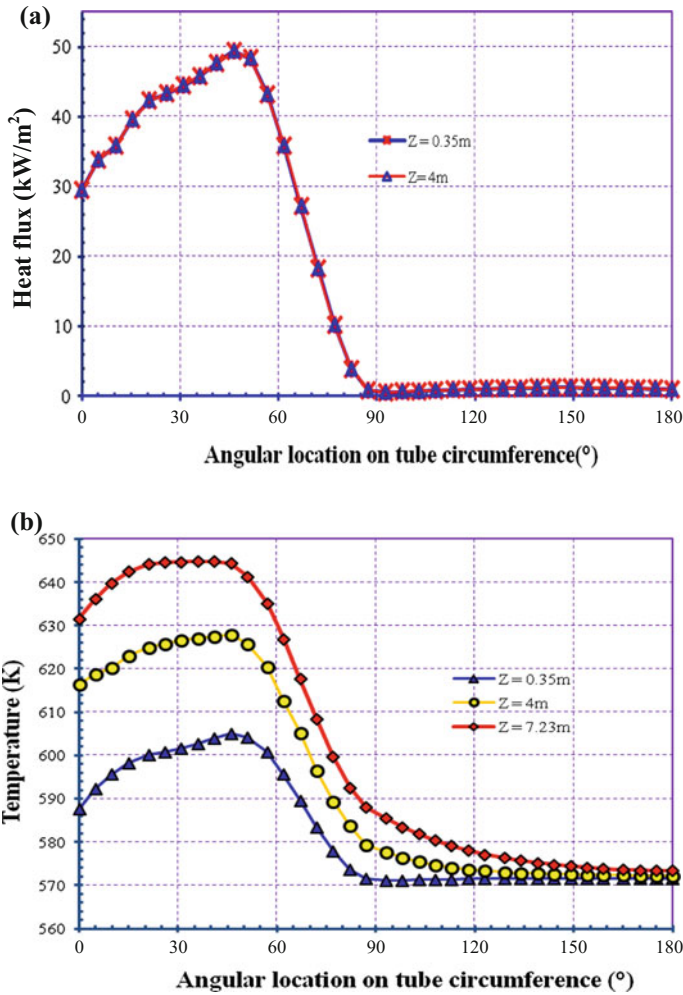
(a)

(b)

Fig. 12 Thermal characteristics along the circumference of the computational domain: **a** resultant heat flux profile, and **b** the temperature profiles (In the figure, 'Z' denotes the longitudinal location on the tube from the inlet end.)

much lower than the residual heat flux in Fig. 12a, which was because of the residual heat flux was calculated for about 1000 W/m^2 DNI and at ideal conditions without considering any heat loss from the surface in contrast to the realistic test conditions as shown in Fig. 5 for validation of the present FV model. Ignoring the discrepancy in the flux magnitude, the similarity of the both profiles confirmed the accuracy of the coupling and the in-house algorithm.

5 Thermal Characteristics of the LS2 Receiver

Using the present FV model, the heat loss from the receiver surface was investigated, and the resultant heat flux profile and the temperature profiles around the receiver surface were calculated as described below.

5.1 Heat Loss Phenomena

As the receiver was bare, and the operating temperature was significantly higher than that of the environment, the receiver must lose heat energy from its outer surface by virtue of temperature difference due to convection and radiation. The individual effect of both of these heat transfer modes was investigated as presented in Table 4.

In the table, the no loss model represents the maximum possible rise of HTF temperature without any heat loss. On the contrary, the total loss model shows the minimum possible temperature rise of the HTF and maximum heat loss at the respective ambient conditions. On the other hand, the convection loss model and the radiation loss model show the effect of convection loss and the radiation loss on the HTF outlet temperature and the heat loss.

As the table shows, from the total loss model, the maximum heat loss increases moderately with the increase of ambient air velocity from 18% of heat energy with 0.1 m/s air velocity to as much as 62% of thermal energy with 9.3 m/s air velocity. The reason for this loss was the convection as could be seen from the convection loss model. Because, in the total loss, the radiation was found to account for around 5% of the heat energy loss, while the convection accounted for the rest of the thermal loss. It should be noted that the radiation loss directly depends on the temperature difference between the receiver and the environment, while the convection loss depends not only on the temperature difference but also on the air velocity of the environment. Therefore, maintaining an optimum evacuation level between the receiver tube and the glass envelop of a conventional PTC is important to proof the convection loss. However, as a higher working temperature would decrease the electric performance of PV solar cells, heat loss from the PV aperture of a CPV/T collector might be beneficial for the cells' efficient operation.

5.2 Resultant Heat Flux and Temperature Profiles of the Receiver Outside Wall

The current model was adapted to calculate the heat flux profile and the temperature profile around the receiver wall at ideal condition. The DNI for this particular
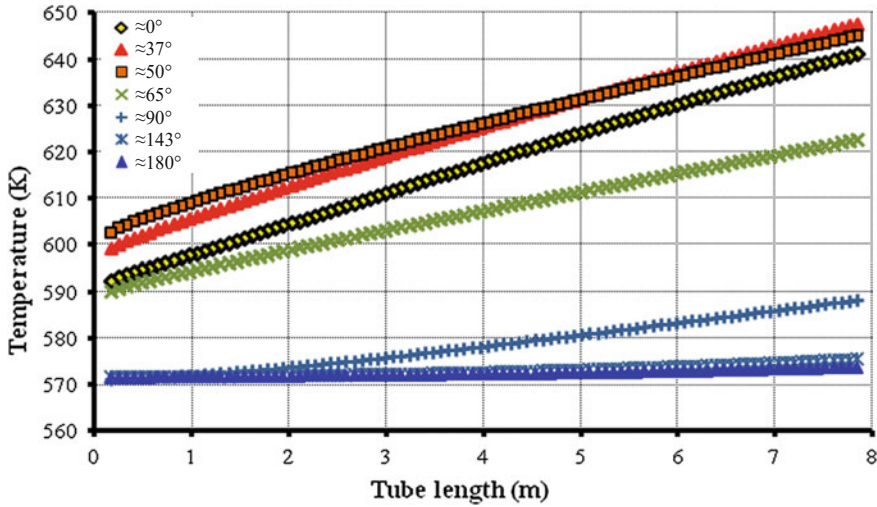
Fig. 13 Longitudinal temperature profile along the length of the tube at different angular locations

investigation was considered about 1 sun. While the circumferential profiles are illustrated in Fig. 12, the longitudinal profiles are presented in Fig. 13.

As the Fig. 12a shows, the heat flux profiles at 0.35 m length location and at 4 m length location of the receiver along the circumference were calculated that were found highly nonuniform and almost similar to that of the solar irradiance distribution. Since both the profiles were coincident, there was no or little variations in heat flux could be seen along the receiver length, which was reasonable as the incident solar flux along the length was assumed uniform.

Again Fig. 12b shows the temperature profiles along the circumference of the receiver at 0.35, 4 and 7.23 m length locations. The temperature profiles were found significantly nonuniform as was found for the heat flux profiles. Unlike the heat flux profile, the temperature was found to increase from the inlet to the outlet along the length of the tube, which was further supported from the longitudinal temperature profile of the receiver as shown in Fig. 13. The increase in temperature, as the figure shows, from inlet to outlet edges of the receiver was found fairly linear.

For a standard PTC, the solar flux distribution along the receiver was found almost fixed. Therefore, it would be possible to decrease the temperature variations along the receiver circumference by increasing the HTF turbulence or HTF mixing inside the domain. The mixing of the HTF inside the receiver could be achieved by using some type of swirl generator such as twisted tape insert into the domain. The insert would induce a swirl or rotation effect into the fluid, so that the HTF may rotate at least 90° while flowing from the inlet to the outlet. By this way, the HTF inside the receiver tube would be heated more evenly, and the resultant temperature profile of the tube wall along the periphery might be gentler, which would not only increase the heat gain of the HTF but also would decrease the heat loss from the receiver surface.

6   Conclusions

A 3-dimensional CCHT model of the receiver tube of a standard PTC was developed applying FV technique of CFD, integrating MCRT optical model. The purpose of the modelling was to explain a method for studying heat transfer mechanism of a receiver system that is exposed to the surroundings under the actual optical and environmental conditions. Accomplishment of the modelling allows predicting energy gain and energy loss potentials of the collector in practice.

In order to be able to validate the FV model directly, the bare receiver tube of the LS2 collector was simulated, as the measured thermal efficiency data of the collector is available in the literature. The Reynolds ratio, Re_r (ratio of Reynolds number to a critical Reynolds number, 4000) of the selected test conditions were varied between 1.6 and 3.74. The heat flux wall was absorbing a nonuniformly distributed concentrated solar radiation, the distribution of which was calculated using the MCRT optical simulation model. The irradiance profile around the circumference of the computational domain was simulated applying MCRT technique and integrated with the FV model using an in-house macro. Radiation and convection loss from the outer surface of the receiver were incorporated in the macro.

The FV model was verified by comparing the calculated and measured HTF outlet temperature data. The absolute deviation between the numerical results and the measured data was estimated would be maximum 2.92%, minimum 0.23% and average 1.11%. This very good agreement between the simulation results and the experimental data confirmed the reliability of the FV model and the accuracy of the MCRT-FV integration.

The FV model was further used to investigate the combined and separate effects of convection heat loss and radiation heat loss. The combined heat loss was found increasing from 19 to 62% of maximum heat gain with the increase of air velocity from 0.1 m/s to 9.3 m/s. Among these losses, radiation loss was accountable for at most 6% of total loss, whereas the convection loss was accountable for the rest of the heat losses that refer to the importance of evacuated glass envelope around the receiver tube of a PTC. On the other hand, the resultant heat flux profiles and the temperature profiles along the periphery of the computational domain were found mostly similar to that of the incident irradiance distribution around the same receiver. While the resultant heat flux was found to be uniform along the length of the tube due to the uniform incident irradiance along the same direction, the temperature was found to gradually increase from the inlet to the outlet.

The convection heat loss from the outer surface of the receiver tube of a PTC with damaged or removed glass envelop was observed very high, because, it is potentially exposed to very high-temperature gradient with respect to the surroundings. Therefore, it is obvious that the receiver tube of a PTC should be enveloped properly with an evacuated glass tube. A well-managed and efficiently operated parabolic trough collector solar energy field could be the best candidate for sustainable energy management of a sustainable future.

References

1. Grena, R. (2009). Optical simulation of a parabolic solar trough collector. *International Journal of Sustainable Energy, 29*(1), 19–36.
2. Yang, B., Zhao, J., Xu, T., & Zhu, Q. (2010). Calculation of the concentrated flux density distribution in parabolic trough solar concentrators by monte carlo ray-trace method. In: *Photonics and Optoelectronic (SOPO) Symposium.*
3. Molla, M. M., Saha, S. C., & Hossain, M. A. Radiation effect on free convection laminar flow along a vertical flat plate with streamwise sinusoidal surface temperature. *Mathematical and Computer Modelling*, *53*(5–6), 1310–1319.
4. Vafai, K., Desai, C. P., Iyer, S. V., & Dyko, M. P. (1997). Buoyancy induced convection in a narrow open-ended annulus. *Journal of Heat Transfer, 119*(3), 483–494.
5. Hamad, F. A., & Khan, M. K. (1998). Natural convection heat transfer in horizontal and inclined annuli of different diameter ratios. *Energy Conversion and Management, 39*(8), 797–807.
6. Dyko, M. P., Vafai, K., & Mojtabi, A. K. (1999). A numerical and experimental investigation of stability of natural convective flows within a horizontal annulus. *Journal of Fluid Mechanics, 381,* 27–61.
7. Borjini, M. N., Mbow, C., & Daguenet, M. (1999). Numerical analysis of combined radiation and unsteady natural convection within a horizontal annular space. *International Journal of Numerical Methods for Heat and Fluid Flow, 9*(7), 742–764.
8. Farinas, M. I., Garon, A., St-Louis, K., & Lacroix, M. (1999). Study of heat transfer in horizontal bare and finned annuli. *International Journal of Heat and Mass Transfer, 42*(21), 3905–3917.
9. Dudley, V. E., Kolb, G. J., Mahoney, A. R., Mancini, T. R., Matthews, C. W., Sloan, M., & Kearney, D. (1994). *Test results: Segs ls-2 solar collector*, 139.
10. Forristall, R. (2003). *Heat transfer analysis and modeling of a parabolic trough solar receiver implemented in engineering equation solver*. National Renewable Energy Laboratory, 1617 Cole Boulevard, Golden, Colorado 80401–3393, Technical report No. NERL/TP-550-34169.
11. Kassem, T. (2007). Numerical study of the natural convection process in the parabolic-cylindrical solar collector. *Desalination, 209*(1–3), 144–150.
12. Reddy, K., Kumar, K. R., & Satyanarayana, G. (2008). Numerical investigation of energy-efficient receiver for solar parabolic trough concentrator. *Heat Transfer Engineering, 29*(11), 961–972.
13. Reddy, K., & Satyanarayana, G. (2008). Numerical study of porous finned receiver for solar parabolic trough concentrator. *Engineering applications of computational fluid mechanics, 2* (2), 172–184.
14. Reddy, K., & Kumar, N. S. (2009). An improved model for natural convection heat loss from modified cavity receiver of solar dish concentrator. *Solar Energy, 83*(10), 1884–1892.
15. Odeh, S. D., Morrison, G. L., & Behnia, M. (1998). Modelling of parabolic trough direct steam generation solar collectors. *Solar Energy, 62*(6), 395–406.
16. Hou, Z., Zheng, D., Jin, H., & Sui, J. (2007). Performance analysis of non-isothermal solar reactors for methanol decomposition. *Solar Energy, 81*(3), 415–423.
17. He, Y.-L., Xiao, J., Cheng, Z.-D., & Tao, Y.-B. (2011). A mcrt and fvm coupled simulation method for energy conversion process in parabolic trough solar collector. *Renewable Energy, 36*(3), 976–985.

18. Cheng, Z., He, Y., & Cui, F. (2013). A new modelling method and unified code with mcrt for concentrating solar collectors and its applications. *Applied Energy, 101,* 686–698.

19. Islam, M., Karim, A., Saha, S. C., Miller, S., & Yarlagadda, P. K. (2012). Three dimensional simulation of a parabolic trough concentrator thermal collector. In: *The Proceedings of the 50th annual conference, Australian Solar Energy Society (AuSES), 6–7 December*. Swinburne University of Technology, Melbourne, Australia.

20. Islam, M., Karim, A., Saha, S. C., Yarlagadda, P. K., Miller, S., & Ullah, I. (2012). Visualization of thermal characteristics around the absorber tube of a standard parabolic trough thermal collector by 3d simulation. In: *the Proceedings of the 4th International Conference on Computational Methods (ICCM2012), November 25–27*. Gold Coast, Australia.

21. Islam, M., Karim, A., Saha, S. C., Miller, S., & Yarlagadda, P. K. (2013). Development of optical ray tracing model of a standard parabolic trough collector. In: *The Proceedings of the Renewable Energy for Sustainable Development & Decarbonisation, World Renewable Energy Congress—Australia 2013, 14–18 July*. Murdoch University, Perth, Western Australia, Australia.

22. Islam, M., Karim, M. A., Saha, S. C., Miller, S., & Yarlagadda, P. K. D. V. (2014). Development of empirical equations for irradiance profile of a standard parabolic trough collector using monte carlo ray tracing technique. *Advanced Materials Research*. Energy Development 860–863, 180–190.

23. ANSYS, I. (2011). *Ansys fluent theory guide*. SAS IP, Inc.: U.S.A.

24. Launder, B. E., & Spalding, D. B. (1974). The numerical computation of turbulent flows. *Computer Methods in Applied Mechanics and Engineering, 3*(2), 269–289.

25. Cheng, Z. D., He, Y. L., Cui, F. Q., Xu, R. J., & Tao, Y. B. (2012). Numerical simulation of a parabolic trough solar collector with nonuniform solar flux conditions by coupling fvm and mcrt method. *Solar Energy, 86*(6), 1770–1784.

26. Cheng, Z. D., He, Y. L., Xiao, J., Tao, Y. B., & Xu, R. J. (2010). Three-dimensional numerical study of heat transfer characteristics in the receiver tube of parabolic trough solar collector. *International Communications in Heat and Mass Transfer, 37*(7), 782–787.

27. Sharples, S., & Charlesworth, P. S. (1998). Full-scale measurements of wind-induced convective heat transfer from a roof-mounted flat plate solar collector. *Solar Energy, 62*(2), 69–77.

28. Leonard, B. P., & Mokhtari, S. (1990). Beyond first-order upwinding: The ultra-sharp alternative for non-oscillatory steady-state simulation of convection. *International Journal for Numerical Methods in Engineering, 30*(4), 729–766.

29. Saha, S. C., Patterson, J. C., Lei, C. Scaling of natural convection of an inclined flat plate: Sudden cooling condition. *Journal of Heat Transfer*, *133*(4), 041503.